*metals*

MDPI

*Article*

# Study of Corrosion Performance and Mechanisms of P91, 304SS and IN625 Alloys in Molten Nitrate Salts Used for Thermal Energy Storage System

**Ning Li [1,2], Naeem ul Haq Tariq [3], Botao Han [1,2], Rui He [1,2], Jiqiang Wang [1], Xinyu Cui [1,*] and Tianying Xiong [1,*]**

[1] Institute of Metal Research, Chinese Academy of Sciences, 72 Wenhua Road, Shenyang 110016, China
[2] School of Materials Science and Engineering, University of Science and Technology of China, 72 Wenhua Road, Shenyang 110016, China
[3] Department of Metallurgy and Materials Engineering, Pakistan Institute of Engineering and Applied Sciences (PIEAS), Nilore, Islamabad 45650, Pakistan
* Correspondence: xycui@imr.ac.cn (X.C.); tyxiong@imr.ac.cn (T.X.)

**Abstract:** The corrosion performance of P91, 304SS and IN625 alloys was evaluated in simulated Solar Salt at 565 °C for up to 15 days. Results revealed that IN625 exhibited the best corrosion resistance with the evolution of thin and compact dual-structured oxide scales. 304SS experienced a great corrosion rate at the initial stage, but showed protective behavior in the later period. A linear mass gain rate was observed for P91, which may result in breakaway corrosion during prolonged immersion time. Finally, the underlying corrosion mechanisms were revealed, providing important guidelines for selecting applicable materials for corrosion mitigation in thermal energy storage (TES) system.

**Keywords:** performance evolution; corrosion mechanism; molten nitrate salt; thermal energy storage; concentrated solar power



**Citation:** Li, N.; Tariq, N.u.H.; Han, B.; He, R.; Wang, J.; Cui, X.; Xiong, T. Study of Corrosion Performance and Mechanisms of P91, 304SS and IN625 Alloys in Molten Nitrate Salts Used for Thermal Energy Storage System. *Metals* **2023**, *13*, 806. https://doi.org/10.3390/met13040806

Academic Editor: George A. Pantazopoulos

Received: 20 March 2023
Revised: 16 April 2023
Accepted: 17 April 2023
Published: 20 April 2023



## 1. Introduction

Renewable energy technologies have gained increasing interest due to ever-growing concerns for global warming and carbon emissions caused by traditional fossil fuel-based energy sources. Among different renewable energy technologies, concentrated solar power (CSP) is a promising technology with certain advantages (low power generation cost, better power distribution ability, etc.) over its counterparts. Therefore, CSP has received great technological interest and commercial investments in the last decade [1]. The CSP plants generally consist of a solar energy receiver, a two-tank storage system, and an electricity generator as schematically shown in Figure 1 [2]. Based on basic principles, the solar radiation is concentrated in a central tower receiver by orderly distributed mirrors (heliostats), and the solar heat is absorbed by heat transfer fluid (HTF) flowing in the receiver which is finally transferred to the hot storage tank. When flowing through the heat exchanger, thermal energy (stored in hot HTF) is utilized to generate steam for driving an ordinary turbine generator. Subsequently, the HTF is transported to the cold storage tank and sent back to the receiver to repeat the cycle. By coupling with a TES system, the CSP plant can store excess solar heat during the daytime and discharge it in high-demand periods, thus resulting in high generation capacity, round-trip efficiency, dispatchability, and reliability [3,4].

In the TES system, HTF and thermal storage medium are considered the most important parts determining thermal efficiency, storage capacity, and cost. To date, various molten salts based on nitrates, nitrites, carbonates, and chlorides have been considered potential candidates for thermal storage medium owing to their high specific heat, high thermal conductivity, high boiling point, low vapor temperature, and high density [1,5–7].

Among them, a binary eutectic mixture of 60 wt.% $NaNO_3$-40 wt.% $KNO_3$ (hereafter referred to as Solar Salt) has been extensively employed in modern CSP plants due to its low melting point, high thermal stability, and wide operation temperature range of 290–565 °C, as summarized in Table 1 [8,9]. Despite the superior advantages, the full potential of TES has not yet been realized because of the main obstacle in selecting reliable materials that can maintain long-term durability in a high-temperature molten salt environment. Most of the TES components are made of metallic alloys which are inevitably susceptible to corrosion in such hostile environments [2,4,10]. Corrosion of metallic materials in molten salts mainly depends on their resistance and salt properties such as type of components, impurity content, and temperature [11]. At high temperatures, molten salts act as ionic electrolytes leading to the convenient transportation of oxidants to a metal surface and the generation of metal oxides. Consequently, alloy materials may either form a compact oxide layer (which could slow down the corrosion rate), or form a non-protective layer (which contains defects or is prone to degradation through delamination, dissolution, and evaporation). After the corrosion environment is designated, the corrosion performance of alloys will rely on their inherent composition and structure.

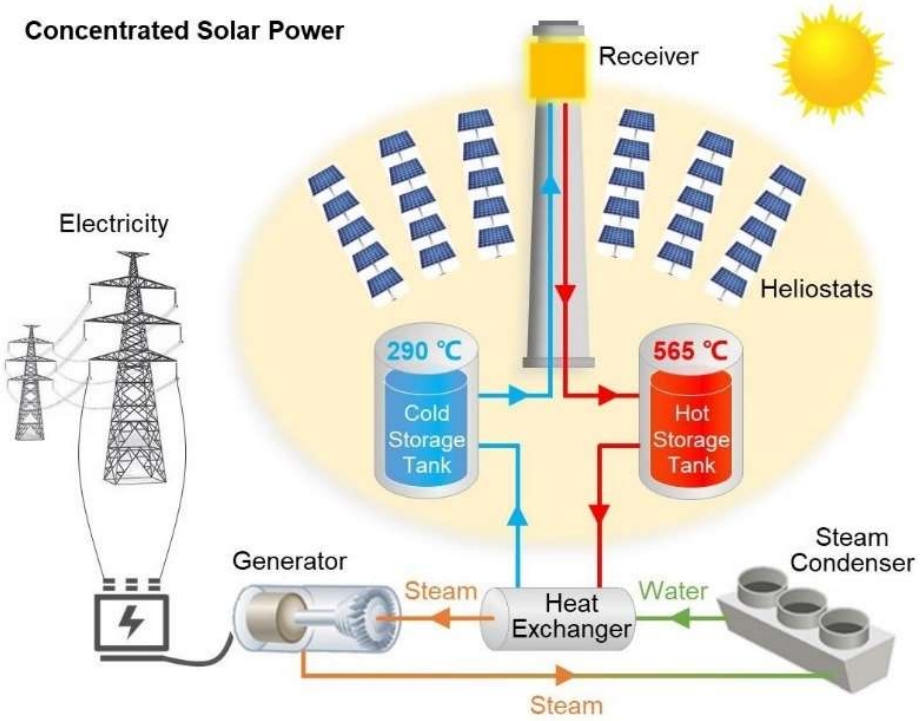


**Figure 1.** Schematic configuration of concentrated solar power technology.

**Table 1.** Thermal and physical properties of various types of molten salt mixtures proposed for TES systems [8,9].

| Salt Composition (in wt.%) | Melting Point (°C) | Stability Limit (°C) | Heat Capacity (J/g/K) | Thermal Conductivity (W/m/K) | Density (kg/L) |
|---|---|---|---|---|---|
| $NaNO_3$ (60)-$KNO_3$ (40) | 220 | 600 | 1.52 | 0.55 | 1.71 |
| $NaNO_3$ (7)-$KNO_3$ (53)-$NaNO_2$ (40) | 142 | 535 | 1.56 | 0.2 | 1.69 |
| $NaNO_3$ (7)-$KNO_3$ (45)-$Ca(NO_3)_2$ (48) | 120 | 500 | 1.45 | 0.52 | 1.83 |
| $Li_2CO_3$ (32.1)-$Na_2CO_3$ (33.4)-$K_2CO_3$ (34.5) | 398 | 800–850 | 1.61 | - | 2.00 |
| NaCl (7.5)-KCl (23.9)-$ZnCl_2$ (68.6) | 204 | 850 | 0.81 | 0.325 | 2.40 |

For molten nitrate salts, numerous studies have been conducted to evaluate the corrosion resistance of various alloys which can be classified into four categories: (1) carbon steel, (2) low-alloy steel, (3) stainless steel, and (4) Ni-based alloy. Carbon and low-alloy steels are the early candidates for the TES components being in contact with molten salts due to their sufficient mechanical properties and low cost [12,13]. Baraka et al. [14] investigated the effect of temperature on the corrosion rate of mild steel in $NaNO_3$-$KNO_3$ eutectic mixture at temperatures ranging from 250 °C to 450 °C for 8 h. They found parabolic and linear corrosion rate laws at lower and higher temperatures, respectively. As a most popular pressure vessel grade of steel, A516 gr. 70 was selected to construct a cold storage tank in Solar Two and some other projects [5,10]. Correspondingly, abundant corrosion investigations have been performed on A516 gr. 70 alloy in nitrate salts at low and moderate temperatures employing static and dynamic immersion equipment or operational storage tanks [15–17]. The results confirmed the detrimental effect of chloride impurity and the restricted applicability of A516 gr. 70 alloy at a temperature above 400 °C. Considering more severe corrosive environment for a hot storage tank and some transport components, low-alloy steels (P91, X20CrMoV11-1 and P92) [18–21], stainless steels (304, 316, 321 and 347) [22–25], and nickel alloys (Haynes 230, Incoloy 800 and Inconel 625) [26–31] were tested in similar experimental conditions. Among them, the last two classes of high chromium alloys were identified as more corrosion-resistant. As is well known, chromium-containing materials and coatings have been widely used in high-temperature oxidation and hot corrosion environments due to the formation of compact and protective oxide scales (rich in chromium) [32–34]. However, the influence of chromium is controversial in a molten nitrate salts environment, since both chromium and chromium oxide have been reported to be unstable and dissolvable under this scenario [35,36].

Considering the conflicting concept, it is interesting to further investigate and ascertain the effect of chromium and its synergistic action with other metal elements (e.g., Fe, Ni) in molten nitrate salts. Further, in most of the published studies, corrosion resistance was characterized generally based on the samples subjected to the longest exposure to molten salts [37]. From the perspective of industrial application, the results and conclusions drawn from these studies are constructive and representative. However, pursuing the performance in a large time span would inevitably miss some detailed information about the performance evolution of corrosion products in a shorter period. Especially, the alloys would undergo a complex and changeable process at the early stage of exposure. This process and corresponding corrosion mechanisms have not been reported yet for most of the alloys.

Therefore, the purpose of this work was to systematically study the evolution of corrosion products formed on different classes of engineering alloys throughout the corrosion process, and discuss the underlying corrosion mechanisms to identify appropriate materials for the TES system. For this purpose, the corrosion behavior of three kinds of alloys, i.e., low-alloy steel (P91), stainless steel (304SS), and nickel alloy (IN625), was evaluated during isothermal exposure in Solar Salt for 1, 3, 5, 7, 9, 12, and 15 days at 565 °C. The exposed samples were analyzed at each immersion interval by gravimetric, macroscopic, microscopic, and crystallographic methods. Moreover, a chemical analysis of the exposed salts was also performed to elucidate the corrosion process.

## 2. Materials and Methods

### *2.1. Preparation of Materials*

Three classes of engineering alloys, i.e., P91, 304SS and IN625, were studied as candidate materials for TES components in contact with molten nitrate salts. The composition of as-received alloys is listed in Table 2. Rectangular samples, with dimensions of $15 \times 10 \times 5$ mm$^3$, were cut by electric discharge machining and then ground with 240 grit SiC abrasive paper to obtain a homogeneous surface. In the next step, samples were degreased with alcohol and finally dried in warm air. Before corrosion tests, the prepared

specimens were stored in a desiccator and weighed by an electronic analytical balance with an accuracy of 0.01 mg.

**Table 2.** Chemical composition (in wt.%) of as-received P91, 304SS, and IN625 alloys.

| Alloy | Fe | Cr | Ni | Mo | Mn | Si | Nb | C | Al | Co |
|---|---|---|---|---|---|---|---|---|---|---|
| P91 | Bal. | 9.00 | 0.20 | 0.96 | 0.50 | 0.42 | 0.09 | 0.10 | - | - |
| 304SS | Bal. | 19.28 | 9.06 | - | 2.00 | 1.00 | - | 0.08 | - | - |
| IN625 | 5.00 | 21.88 | Bal. | 8.75 | 0.50 | 0.50 | 3.94 | 0.10 | 0.40 | 1.00 |

The Solar Salt, a binary salt mixture composed of $NaNO_3$ (60 wt.%) and $KNO_3$ (40 wt.%) (Sinopharm Chemical Reagent Co., Ltd., Shanghai, China) with analytical pure quality, was used as the corrosion medium. The composition of $NaNO_3$ and $KNO_3$ is shown in Table 3. Both salts with corresponding proportions were weighed and mechanically mixed for 2 h. Subsequently, the salt mixture was kept in a drying oven for 3 h at 150 °C to remove moisture in the salts and then preheated at 300 °C for 1 h before the immersion test.

**Table 3.** Composition (in wt.%) of as-received nitrate salts used in this study.

| Salt | Purity | Sulfate | Nitrite | Calcium | Magnesium | Total Chlorine |
|---|---|---|---|---|---|---|
| $NaNO_3$ | 99.4 | <0.003 | <0.0005 | 0.003 | - | <0.0015 |
| $KNO_3$ | 99.6 | 0.003 | 0.001 | 0.004 | 0.0002 | 0.003 |

### *2.2. Corrosion Procedure*

A series of static corrosion tests were conducted in a muffle furnace operating at 565 °C (i.e., the temperature in most hot storage tanks) as graphically presented in Figure 2. Four coupons of each set of samples were immersed in Solar Salt using a 45 mL alumina crucible boat without a sealing lid on it and then heated from 300 °C to 565 °C in 1 h. The molten salt mixture was in direct contact with air in the furnace chamber. After each accumulative immersion time of 1, 3, 5, 7, 9, 12, and 15 days, the corresponding crucible was taken out from the furnace. Subsequently, the salt mixture was removed from the crucible, and coupons were allowed to cool down gently in the crucible to avoid the spallation of oxide scales caused by thermal stress. Four sets of samples were tested simultaneously in a uniform hot zone of the furnace using a specially designed metallic holder. After cooling, the exposed coupons were immersed in hot deionized water for 10 min. The immersion process was repeated three times with fresh water to eliminate the salt residues on the surface of the samples thoroughly. Finally, the coupons were dried for weighing and further characterization.

### *2.3. Characterization of Samples and Salts*

Three coupons of each set of samples were weighted to calculate the average values of mass gain and corrosion rate, and the other one was subjected to macroscopic, microscopic, and structural analysis.

The mass gained by the samples was determined using Equation (1):

$$\Delta m/S_0 = (m_f - m_i)/S_0 \quad (1)$$

where $\Delta m$ is mass change (mg), $m_i$ is the initial mass (mg), $m_f$ is the final mass at any given time (mg) and $S_0$ is the surface area of the sample before corrosion ($cm^2$).

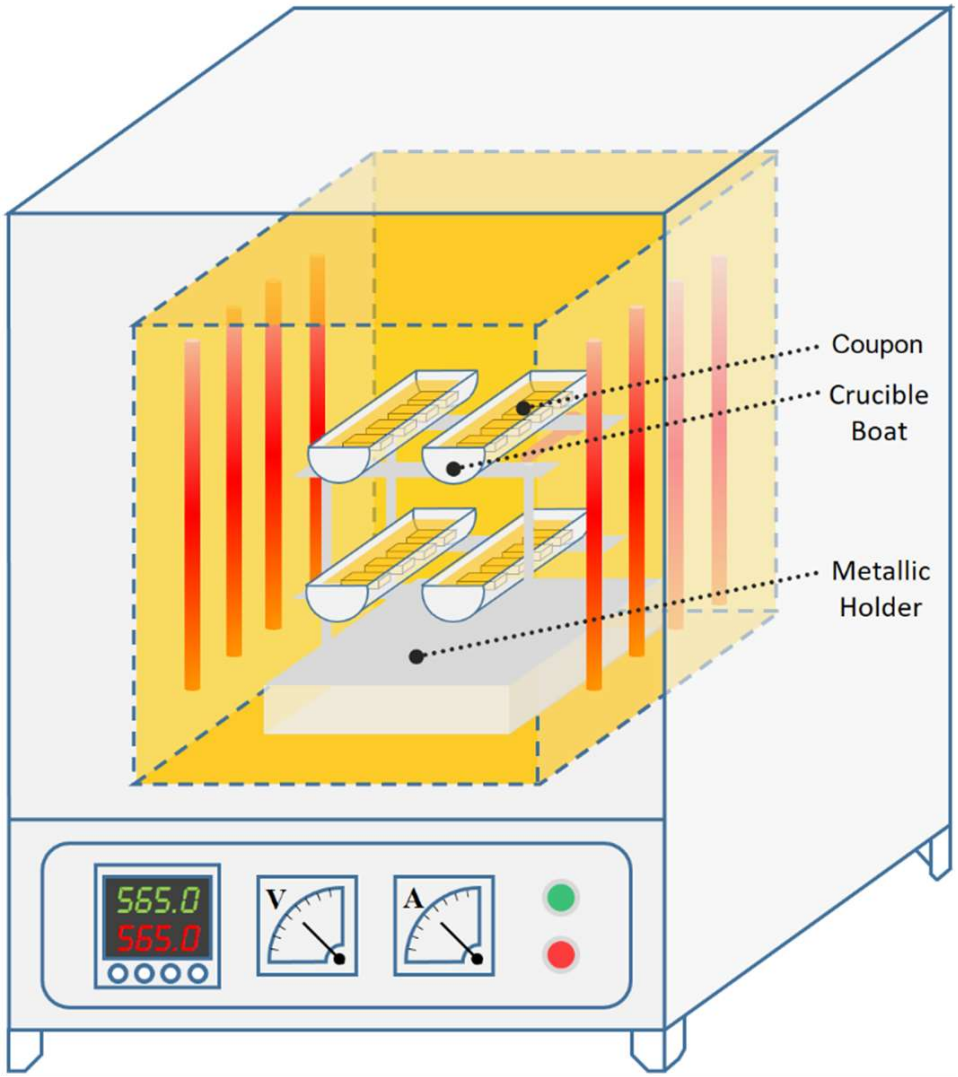


**Figure 2.** Schematic of corrosion test apparatus used in this study.

To accurately measure the corrosion rate of three alloys, the ASTM G1-03 standard [38] was adopted to descale the samples to avoid ambiguities caused by semi-adherent oxide scales. Three coupons of each set of samples were carefully descaled after mass gain measurement using a corresponding chemical aqueous solution which could cause a negligible attack on the parent alloy as demonstrated in several previous studies [24,39]. Using weight loss data, the corrosion rate (CR) for the alloys was calculated by Equation (2):

$$\mathrm{CR}\ (\mu\mathrm{m}\,/\,\mathrm{yr}) = 87{,}600\ \Delta\mathrm{m}/\rho\tau \tag{2}$$

where $\Delta$m is descaled mass loss per unit area (mg/cm$^2$), $\rho$ is the density of alloy (g/cm$^3$): $\rho_{(\mathrm{P91})}$ = 7.85 g/cm$^3$, $\rho_{(\mathrm{304SS})}$ = 7.94 g/cm$^3$ and $\rho_{(\mathrm{IN625})}$ = 8.44 g/cm$^3$, and $\tau$ is the exposure time (h).

Macroscopic, microscopic, and structural analyses were performed to investigate the evolution of oxides on P91, 304SS, and IN625 after each exposure time. To visually examine the surface changes, macrographs of samples were captured after cleaning treatment. Then X-ray diffraction (XRD) was carried out for phase analysis of the corrosion scales using a Philips X'Pert MPD diffractometer with Cu K$\alpha$ radiation. The range of 2-theta was 10–90° and the scanning rate was 20°/min. The obtained diffraction patterns were analyzed by comparing them with the standard database in MDI JADE 6.0 software. To evaluate the details of corrosion products, a surface micrograph at each time point was obtained using

field emission scanning electron microscopy (FESEM, Zeiss Merlin Compact) equipped with energy dispersive spectroscopy (EDS). Subsequently, the coupons used for characterization were embedded individually and ground by using a series of silicon carbide paper followed by polishing with various grades of diamond paste. After the metallographic preparation, the cross-section of samples was characterized using the same FESEM.

Finally, chemical analysis of used salts (collected from the crucibles with the longest exposure time) of three alloys was conducted using Inductively Coupled Plasma Mass Spectrometry (ICP-MS, Agilent 7500ce) to determine the concentration of chromium possibly dissolved from oxides or parent alloy. The collected salt was ground to powder in an agate mortar, and then 0.5 g of powder was weighed and diluted in 50 mL of purified water. The main parameters of ICP-MS were as follows: RF power (1500 W), RF matching (1.67 V), carrier gas flow rate (0.85 L/min), make up gas flow rate (0.21 L/min), and nebulizer pump flow rate (6.0 r/min).

## 3. Results and Discussion

### *3.1. Gravimetric Analysis*

Different mass gain and corrosion rate curves for three alloys are present in Figures 3a and 3b respectively, indicating the occurrence of various corrosion processes and mechanisms for them. Continuous mass gain with a rate constant of $9.04 \times 10^{-3}$ (mg/(cm$^2$·day)) can be noticed for low chromium alloy P91 during the first 12 days of immersion. Subsequently, the weight gain data sharply increases with an average mass gain of 0.36 mg/cm$^2$ for the samples immersed for 15 days in molten salt. The large weight change, resulting at the last interval, implies that the corrosion rate may become even faster with a further increase in the immersion time. This inference seems to be in agreement with the corrosion rate curve presented in Figure 3b. Figure 3b clearly depicts that the corrosion rate of P91 samples, immersed for 1 day, has the highest value of 67.63 µm/a which gradually reduces to the lowest value of 19.73 µm/a for the samples immersed for 12 days. After 12 days, the corrosion rate shows an increase (31.84 µm/a for the samples immersed for 15 days) indicating that the oxide scale formed on P91 may be non-protective and it could not efficiently impede the continuous penetration of oxidant species which ultimately make contact with the underlying matrix. During the last interval, cracks or delamination may appear in the scale thereby providing more convenient access points for oxidant species. Consequently, the corrosion of the internal parent alloy is accelerated.

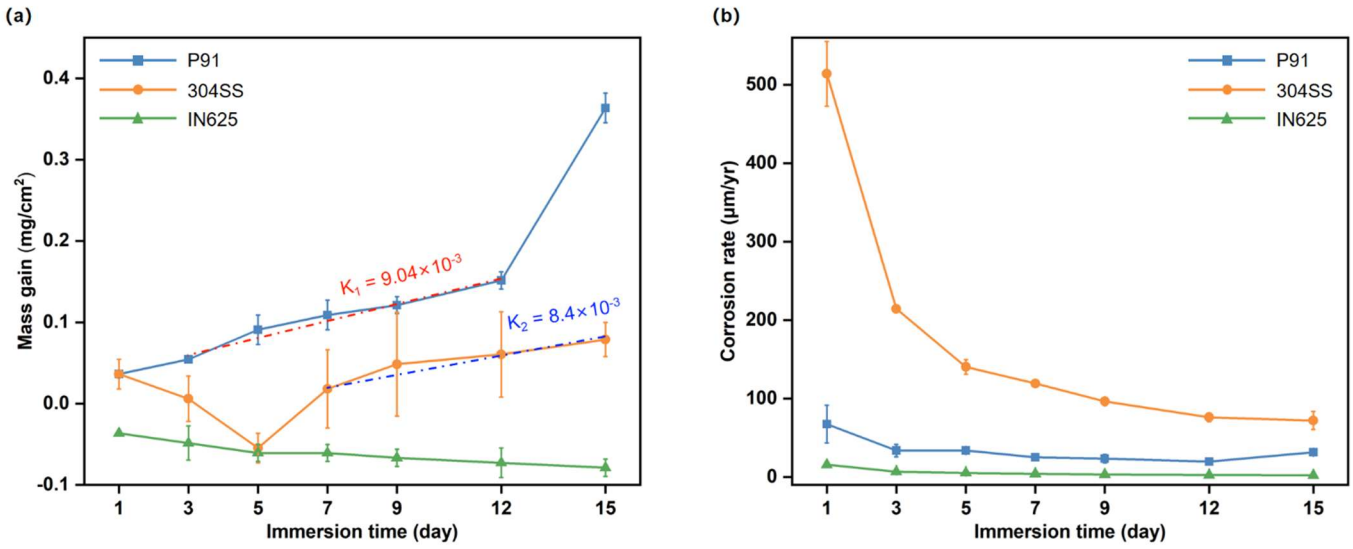


**Figure 3.** (**a**) Mass gain and (**b**) corrosion rate as a function of immersion time for P91, 304SS, and IN625 alloys in Solar Salt at 565 °C.

304SS (with a relatively high content of chromium) exhibits weight loss during the first 5 days of immersion. This behavior implies that the growth of oxide scale and dissolution of oxides or parent alloy may occur simultaneously, and the latter case has a predominant effect on the samples immersed for 5 days. Further, during the early stage of the immersion test, corrosion products on 304SS may be loose thus making them unable to inhibit the direct contact between the underlying matrix and salt mixture. Hence, rapid oxide growth with a high degradation rate of 514.03 μm/a (which is nearly eight times higher than that of P91) takes place for the 304SS samples immersed for 1 day. Therefore, the oxide scale on 304SS is supposed to be much thicker. Interestingly, despite the quite different corrosion rates, the mass gain of P91 and 304SS samples is almost the same after 1 day of immersion, which means 304SS suffered more evident weight loss than P91. It has been reported in the literature [35,40] that chromium can be directly or indirectly dissolved into nitrate salts in the form of chromate ions. It is reasonable to assume that 304SS experienced stronger dissolution of chromium (due to its higher content of chromium as shown in Table 2) than P91. After 5 days of immersion, it starts gaining weight at a rate of $8.4 \times 10^{-3}$. The corresponding mass gain curve exhibits a parabolic mechanism indicating that the growth of corrosion products is controlled by solid-state diffusion of alloying elements and oxidant species. The oxide scale also becomes more compact and protective. Although the corrosion rate of 304SS decreases rapidly after 1 day of immersion, the acquired data of samples, immersed for 15 days, is about two times higher than that of P91.

In contrast, IN625 slowly loses weight during the whole corrosion test with a final mass loss of 0.08 mg/cm$^2$. Further, the alloy results in the lowest corrosion rate (2.27 μm/a for the samples immersed for 15 days) providing the best corrosion-resistant performance among the three alloys. Similar to 304SS, the weight loss behavior of IN625 (containing a higher content of chromium) may be attributed to the predominant dissolution of chromium. However, the oxides formed on IN625 are different from those on 304SS, because IN625 contains a large amount of nickel which is more oxidation resistant than iron as suggested by their electrochemical and thermodynamic potential [41,42]. For IN625, the most of weight loss occurs during the first day of immersion. Afterward, the formed oxides (with corrosion-resistant composition and compact microstructure) seem to effectively hinder the outward diffusion of alloy elements and the inward penetration of oxidant species.

The mass gain and corrosion rate curves for P91, 304SS and IN625 indicate that each alloy may have a specific reaction process. Combined with other complementary analysis methods, the two sets of plots in Figure 3 can further assist in investigating the underlying corrosion mechanisms of the studied alloys.

### *3.2. Macroscopic Observations*

Figure 4 shows the surface appearance of three alloys for each immersion time. The alloys show various evolution of surface morphology and coloration during the whole immersion test. On the surface of P91 and 304SS, the oxides seem to be growing and compacting with immersion time, and the grinding scratches disappear after 7 and 9 days of immersion, respectively. A thin oxide film, with reddish brown color, is initially formed on P91 after 1 day of immersion, which later seems to become thicker and more compact with a darker hue. For 304SS, uniform gray oxides are observed on the surface of the initial two coupons, and later become thinner for the coupon immersed for 5 days. Subsequently, compact oxides (with dim gray color) are formed again covering the whole parent alloy. Further, no signs of scale rumpling, cracking, or spalling are noticed on the surface of P91 and 304SS. This means that the corrosion products may protect the steel substrates to some extent. The colorful appearance of IN625 indicates that the thickness of the surface oxide layer is changing with immersion time. However, after 15 days of immersion, the oxide layer is so thin that grinding trails are still visible. This corresponds well with the gravimetric result that IN625 exhibits the smallest mass change. Oxides on nickel alloy seem to have a better protective effect than those formed on iron alloys, thus making

IN625 the most resistant alloy against molten nitrate salts during the static corrosion test in this study.

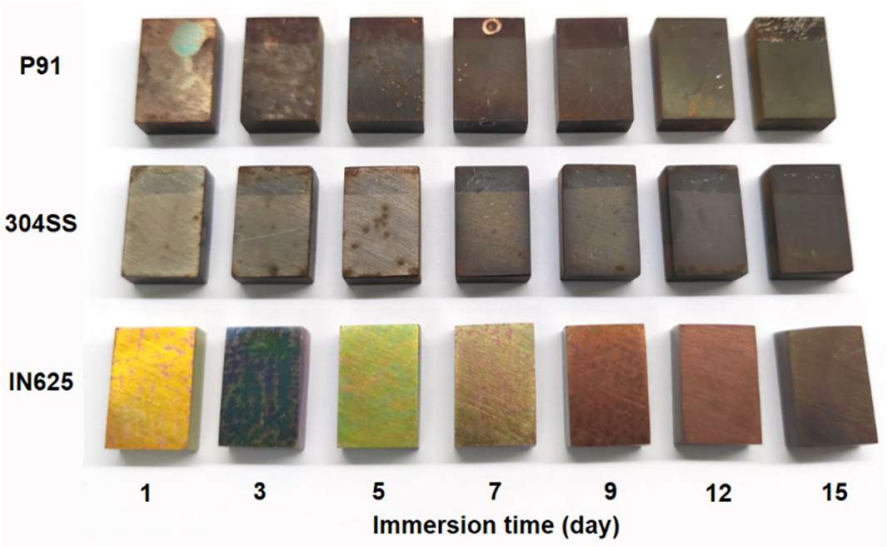


**Figure 4.** Macroscopic appearance of P91, 304SS, and IN625 alloys after 1, 3, 5, 7, 9, 12, and 15 days of exposure to Solar Salt at 565 °C.

### *3.3. XRD Analysis*

The surface phase structures of three alloys during the whole corrosion period were identified by XRD (Figure 5). It is confirmed that the predominant phases in the oxide scale of iron alloys are hematite ($Fe_2O_3$) and magnetite ($Fe_3O_4$) while the ones for the nickel alloy are nickel oxide (NiO) and niobium oxide ($Nb_2O_5$). These types of corrosion products are normally found under molten salts or oxygen-containing atmospheres [32,43,44]. A stable magnetite layer is usually beneficial for mitigating corrosion rate by hindering the outward diffusion of metal ions and inward diffusion of oxide ions [45]. Nickel oxide is less affected and therefore it is considered as a protective oxide layer for nickel alloys or coating to resist molten salt corrosion [46]. It is interesting to note that no chromium oxide ($Cr_2O_3$) appears on the surface of the three alloys even though both 304SS and IN625 contain a high enough content of chromium. This is in good agreement with the literature [22,29]. Moreover, iron-chromium spinel ($FeCr_2O_4$) and nickel-chromium spinel ($NiCr_2O_4$) peaks, with either weak intensity or overlapping with other oxide peaks, can be noticed for two different metal-based (i.e., Fe and Ni) alloys, respectively. It can be inferred that $FeCr_2O_4$ and $NiCr_2O_4$ are likely to exist as an inner oxide layer, covered by the top (depleted chromium) oxide layer. Further, the evolution of peak intensity of the generated oxides indicates that their amount and thickness increase with increasing exposure time. Correspondingly, the peak intensity of the substrate decreases with the thickening of oxide scales. It is interesting to note that the highest peak for 304SS, appearing at a 2 Theta value of 43.6°, changes to 44.6° (i.e., highest peak position for P91) after 1 day of exposure. This phenomenon becomes more evident as corrosion proceeds. The transformation of the primary phase from $Cr_{0.19}Fe_{0.7}Ni_{0.11}$ to Fe-Cr indicates a significant change in surface composition for 304SS. It can be seen in Table 2 that the main difference in the chemical composition of P91 and 304SS is the higher content of Cr and Ni contained in the latter. Combining with gravimetric analysis results, it can be deduced that 304SS has suffered severe dissolution of chromium at the initial stage of corrosion and the surface concentration of Cr decreases to a level similar to P91. However, adequate content of chromium in the underlying oxide layer and matrix could provide better corrosion resistance for 304SS when compared with P91. This will be discussed in detail later in Section 3.4.

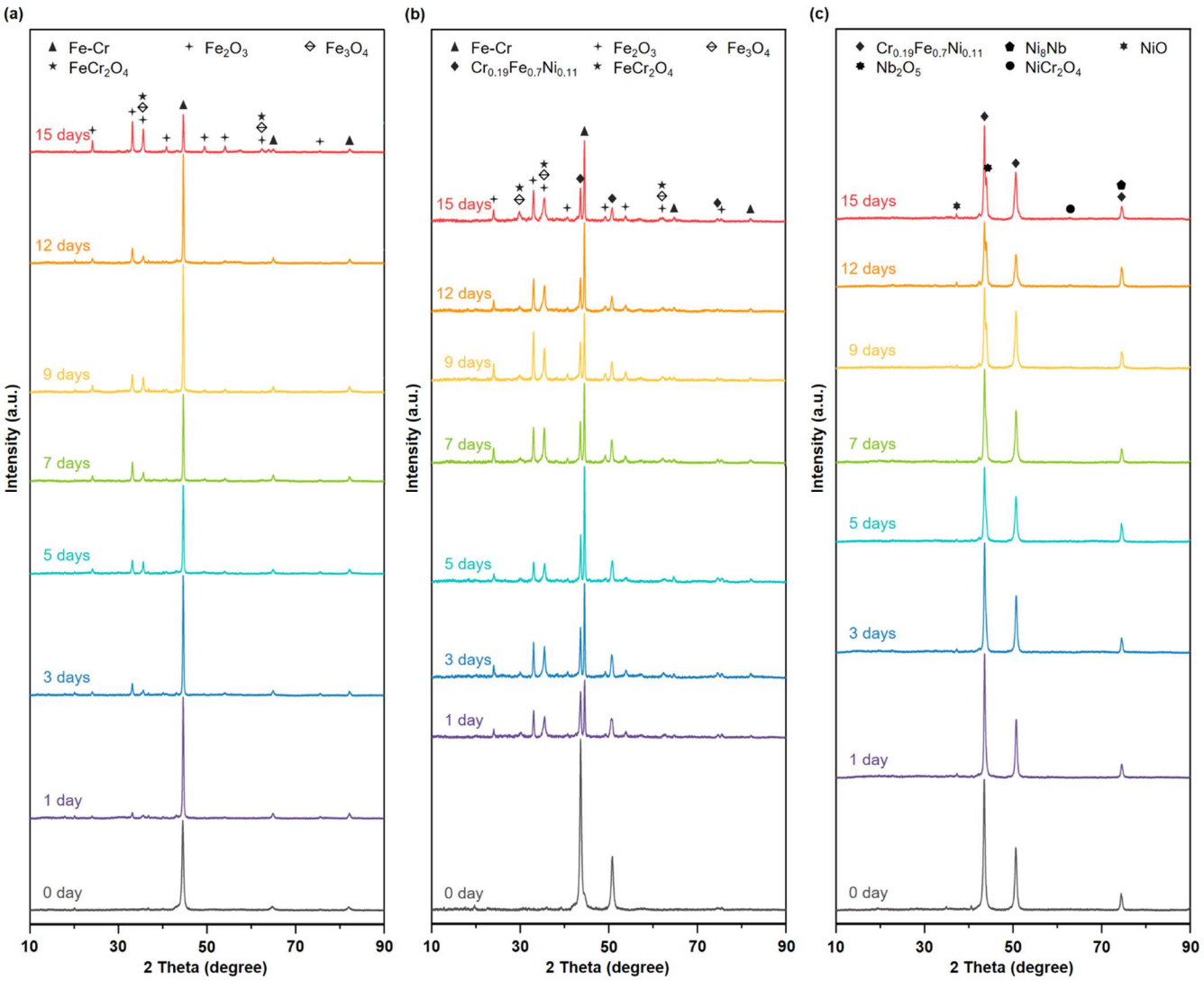


**Figure 5.** XRD patterns of (**a**) P91 and (**b**) 304SS and (**c**) IN625 alloys exposed to Solar Salt at 565 °C for 0 day, 1 day, 3 days, 5 days, 7 days, 9 days, 12 days, and 15 days.

### *3.4. Microscopic Observations*

To further investigate the corrosion products, SEM images of the three alloys (immersed in Solar Salt for different durations) from both surface and cross-sectional perspectives are provided in Figures 6–8. Therein, the distribution of main elements in the corroded layer is shown by EDS line scanning and the composition of marked regions is summarized in Tables 4–6.

**Table 4.** EDS elemental analysis of regions marked in Figure 6 for P91 alloy (in wt.%).

| Region | Fe | Cr | O | Ca | Mn | Si | C | Fe/Cr |
|---|---|---|---|---|---|---|---|---|
| 1 | 83.82 | 8.47 | 0.97 | 0.09 | 0.45 | 0.41 | 5.79 | 9.90 |
| 2 | 76.33 | 5.93 | 16.04 | 0.23 | 0.93 | 0.54 | - | 12.87 |
| 3 | 87.66 | 8.23 | 3.13 | - | 0.50 | 0.48 | - | 10.65 |
| 4 | 73.73 | 5.74 | 19.25 | 0.15 | 0.74 | 0.39 | - | 12.84 |
| 5 | 71.65 | 5.74 | 21.13 | 0.42 | 0.62 | 0.44 | - | 12.48 |
| 6 | 70.91 | 1.60 | 26.23 | 0.81 | - | 0.45 | - | 44.32 |

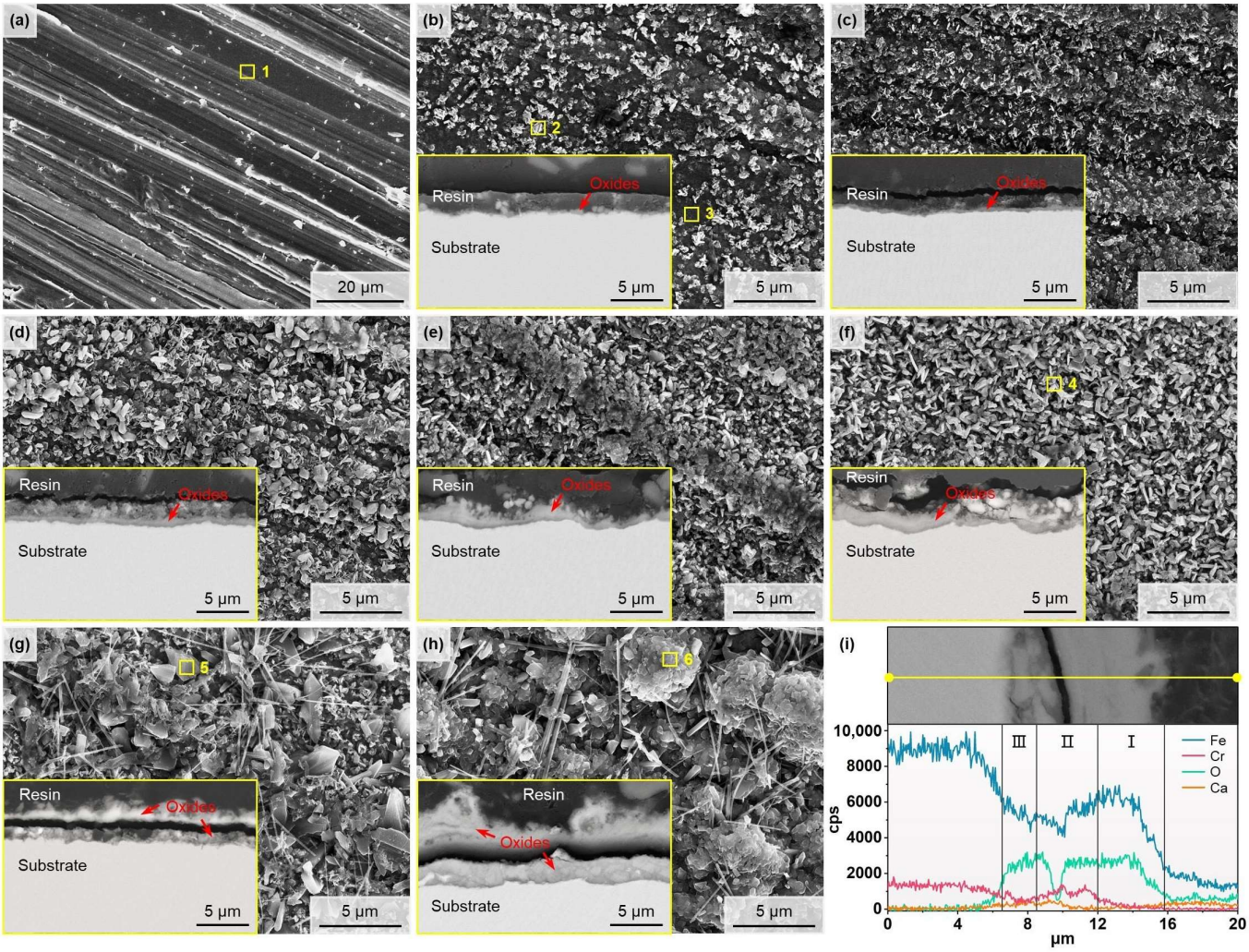


**Figure 6.** Surface and cross-sectional micrographs of P91 alloy exposed to Solar Salt at 565 °C for (**a**) 0 day, (**b**) 1 day, (**c**) 3 days, (**d**) 5 days, (**e**) 7 days, (**f**) 9 days, (**g**) 12 days, and (**h**) 15 days. Panel (**i**) presents a magnified view of the cross-section and corresponding EDS line scanning for the sample immersed for 15 days. NB: The inserts in panels (**b**–**h**) show the cross-sectional view for the corresponding sample.

**Table 5.** EDS elemental analysis of regions marked in Figure 7 for 304SS alloy (in wt.%).

| Region | Fe | Cr | O | Ni | Mn | Si | Ca | Na | Mg | C | Fe/Cr |
|---|---|---|---|---|---|---|---|---|---|---|---|
| 1 | 67.15 | 17.54 | 1.37 | 7.24 | 1.34 | 0.42 | - | - | - | 4.94 | 3.83 |
| 2 | 70.76 | 5.76 | 12.98 | 4.10 | 0.40 | 1.08 | 0.14 | - | 0.08 | 4.70 | 12.28 |
| 3 | 65.96 | 1.89 | 27.04 | - | 0.48 | 0.26 | 0.65 | - | 0.22 | 3.50 | 34.90 |
| 4 | 60.76 | 4.74 | 26.29 | 2.39 | 1.02 | 0.21 | 0.24 | - | 0.30 | 4.05 | 12.82 |
| 5 | 71.19 | 6.18 | 12.90 | 3.47 | 0.41 | 0.69 | 0.07 | - | 0.21 | 4.88 | 11.52 |
| 6 | 63.67 | 1.85 | 26.22 | - | 0.27 | 0.19 | 1.18 | 1.57 | 0.20 | 4.85 | 34.42 |
| 7 | 57.98 | 4.76 | 27.50 | 1.91 | 1.35 | 0.20 | 0.13 | - | 0.06 | 6.11 | 12.18 |
| 8 | 54.04 | 1.61 | 35.72 | - | 0.07 | 0.20 | 0.71 | - | 0.13 | 7.52 | 33.57 |
| 9 | 49.09 | 1.55 | 37.13 | - | 0.62 | 0.20 | 2.56 | 1.82 | 0.12 | 6.81 | 31.67 |
| 10 | 59.47 | 2.20 | 25.77 | 0.96 | 1.12 | - | 2.24 | 3.14 | - | 5.10 | 27.03 |

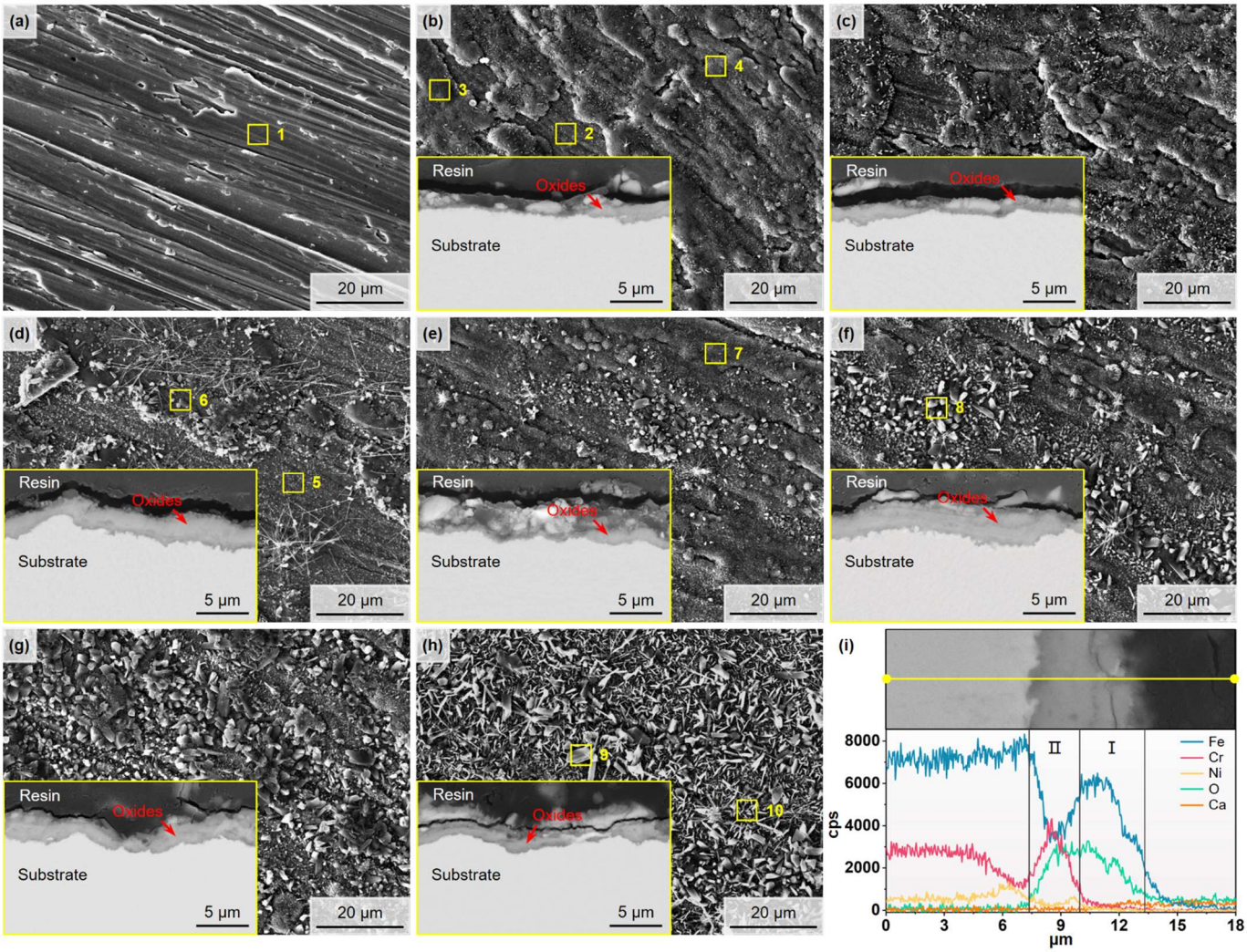


**Figure 7.** Surface and cross-sectional micrographs of 304SS alloy exposed to Solar Salt at 565 °C for (**a**) 0 day, (**b**) 1 day, (**c**) 3 days, (**d**) 5 days, (**e**) 7 days, (**f**) 9 days, (**g**) 12 days, and (**h**) 15 days. Panel (**i**) presents a magnified view of the cross-section and corresponding EDS line scanning for the sample immersed for 15 days. NB: The inserts in panels (**b**–**h**) show the cross-sectional view for the corresponding sample.

**Table 6.** EDS elemental analysis of regions marked in Figure 8 for IN625 alloy (in wt.%).

| Region | Ni | Cr | O | Mo | Fe | Nb | Ca | Na | Si |
|---|---|---|---|---|---|---|---|---|---|
| 1 | 60.08 | 16.69 | 7.71 | 5.74 | 4.38 | 5.01 | - | - | 0.39 |
| 2 | 58.85 | 14.91 | 9.35 | 5.13 | 5.08 | 5.67 | 0.23 | - | 0.78 |
| 3 | 57.85 | 10.79 | 13.43 | 3.84 | 5.66 | 7.78 | - | - | 0.65 |
| 4 | 54.59 | 10.38 | 20.93 | 4.85 | 4.46 | 4.79 | - | - | - |
| 5 | 15.41 | 1.17 | 32.65 | - | 4.00 | 32.26 | 9.61 | 4.90 | - |

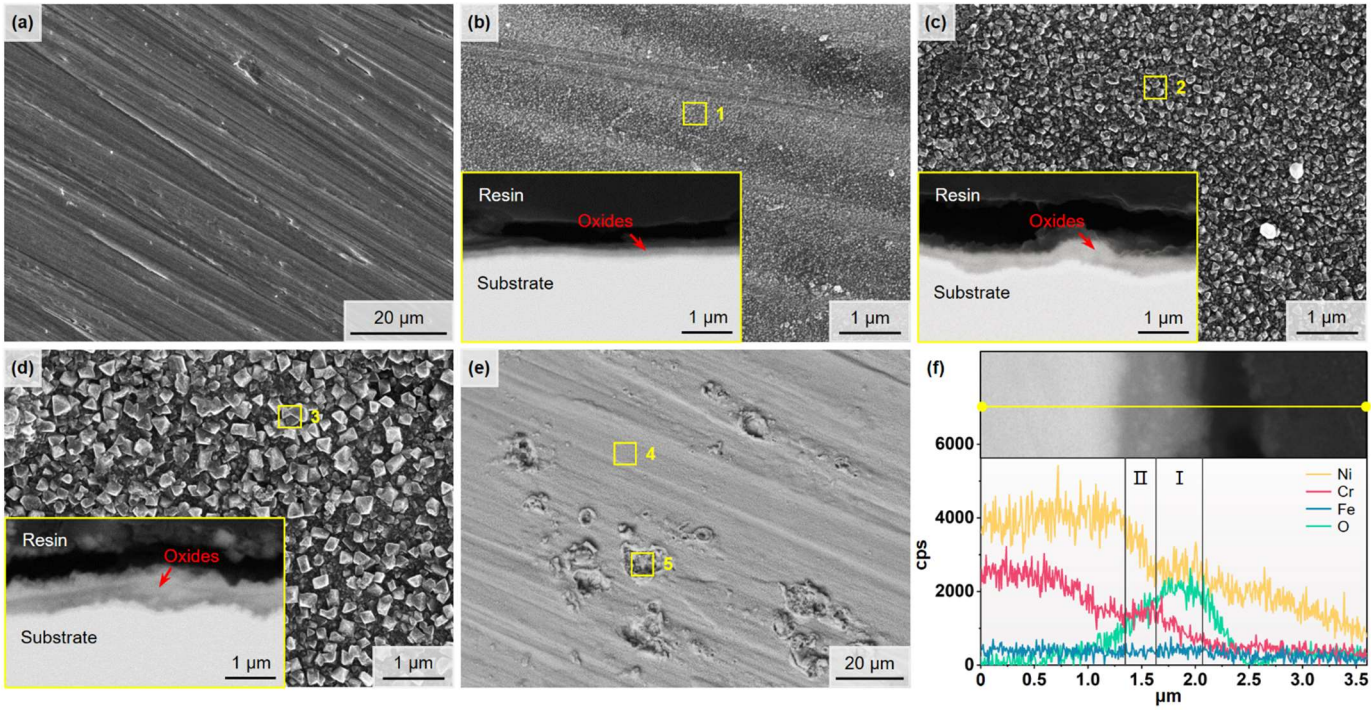


**Figure 8.** Surface and cross-sectional micrographs of IN625 alloy exposed to Solar Salt at 565 °C for (**a**) 0 day, (**b**) 1 day, (**c**) 7 days, and (**d**) 15 days. Panel (**e**) shows a surface micrograph for the sample immersed for 15 days at low magnification. Panel (**f**) presents a magnified view of the cross-section and corresponding EDS line scanning for the sample immersed for 15 days. NB: The inserts in panels (**b**–**d**) show the cross-sectional view for the corresponding sample.

#### 3.4.1. P91 Alloy

Compared with the blank sample shown in Figure 6a, uniformly distributed tiny oxide particles (Region 2 in Figure 6b) appear on the sample immersed for 1 day. These particles are of rod shape with a length of 400 to 500 nm, and are rich in iron and chromium. It seems that, in the early stage of corrosion, some areas are slightly oxidized like Region 3 in Figure 6b. With increasing immersion time, oxide particles accumulate gradually and completely cover up the parent material after 5 days, thus resulting in the formation of a thin (~0.7 μm) continuous scale. This is quite evident in the cross-sectional image provided in the inset of Figure 6d. After 15 days of immersion, the oxide scale achieves a thickness of 9.2 μm and assumes the morphology of a duplex structure composed of a uniform inner layer and an irregular outer layer. As can be seen from the cross-sectional images, the outer layer is prone to delamination during metallographic preparation. The two layers may have different phase structures and elemental compositions. Relevant literature [18,20,47] suggest that an outer layer of $Fe_2O_3$ and an inner layer (composed of $Fe_3O_4$ and Fe-Cr spinel) are always formed on low-alloy steels subjected to molten salts or high temperature atmosphere. The EDS analysis of the sample immersed for 15 days shows that the oxide scale is mainly divided into three distinct regions, i.e., (I) an iron oxide outer layer, (II) a Cr-rich region near the outer oxide layer, and (III) a Cr-depletion zone adjacent to the substrate. Generally, the Fe-Cr spinel layer is considered as a protective film for the underlying matrix. Thus, it is anomalous to find a Cr-depleted oxide layer inside the iron-chromium oxide region, which implies that the Fe-Cr spinel layer formed on P91 could not effectively impede the penetration of oxidants during the immersion test. This inference coincides well with the linear mass gain rate of P91 in Figure 3a. Further, the inference suggests that a thick multilayered oxide scale (composed of alternating iron oxide and iron-chromium oxide layers) may be formed on the P91 sample for prolonged exposure to molten nitrate salts. In case of no spallation, the scale will be further thickening. Consequently, the corrosion rate is reduced due to the increase in migration distance

for oxidants and metal ions. However, under a dynamic corrosion condition, the alloy may suffer a faster rate of degradation owing to the probable erosion and the spallation of the oxide scale. In addition, the growth stress of oxides (caused by dissimilar phase structures) may generate cracks which will provide easy access to oxidants thus resulting in breakaway corrosion.

The chemical composition of six surface regions (marked in Figure 6) is listed in Table 4 and the mass ratio of iron and chromium is provided to show their relative change with immersion time. Regions 2, 4 and 5 in Figure 6 contain oxide particles generated at different stages, respectively. They have similar content of iron and chromium but with increasing content of oxygen. It is speculated that they might be Fe-Cr spinel particles rich in iron. In the case of Region 5, more content of oxygen and calcium is detected when compared with those of Regions 2 and 4 in Figure 6. This difference in composition may be associated with the bigger-size and angular oxides in Region 5. Region 6 contains the oxides of the outer layer which is rich in iron with a trace of chromium, indicating that the outer layer is mainly composed of iron oxides after 15 days of immersion.

#### 3.4.2. 304SS Alloy

Contrary to the P91 sample, a clear oxide scale (with a maximum thickness of 1.6 µm) is formed on 304SS after 1 day of immersion as shown in Figure 7b. Clearly, most of the surface is covered by thick corrosion products. And a few areas, like Region 2 in Figure 7b, are slightly corroded. Combining with the elemental analysis provided in Table 5, the thick corrosion scale is either composed of iron oxides (Region 3 in Figure 7b) or the aggregates of abundant tiny oxide particles (Region 4 in Figure 7b) which are observed on the surface of P91. However, the scale formed on the 304SS sample (immersed for 1 day) seems to be more compact as compared to that of P91 (immersed for several initial durations). Besides, it contains more oxygen and less chromium, which indicates that 304SS has suffered more severe oxidation and dissolution of chromium during the first day of immersion. Figure 7a–h confirm that the evolution of surface morphology is in line with the mass change result presented in Figure 3a. After 1 day, the oxide scale is thinning and partially peels off exposing more subscales like Region 5 in Figure 7d. The subscale is directly oxidized as soon as the spallation of the surface scale takes place, and shows a similar morphology with the P91 sample immersed for 1 day. Despite there are some residual oxide islands (Region 6 in Figure 7d) and the generation of new oxide scale could cause mass increment, the significant loss of initially formed oxide dominates the net mass change of the fifth-day sample (Figure 3a). After 7 days of exposure, the new oxides (Region 7 in Figure 7e) completely cover up the sample while a few sporadic coarse particles (Region 8 in Figure 7f) are noticed on the surface. Subsequently, the coarse particles (which seem to be over-oxidized $Fe_2O_3$ with a trace of calcium) gradually spread over the top surface. It can be seen that the surface of the final group of coupons is fully covered with calcium-rich oxide particles (Regions 9 and 10 in Figure 7h) with an average size of 2 to 3 µm. Combining with the XRD result, Fe-Cr becomes the primary surface phase for 304SS after transient immersion, exhibiting a similar corrosion behavior with P91 at later stages of the immersion test. This can be verified by the similar morphology and composition of oxide scales formed on P91 and 304SS (at later stages). Hence, from the perspective of oxide scale formation, it is reasonable to assume that 304SS experiences two types of corrosion mechanisms in molten Solar Salt at 565 °C. In the first process, the dissolution of chromium (accompanied by the massive oxidation of iron) and the spallation of iron oxide scale quickly take place during the initial stages of the immersion test. In the second mechanism, occurring at about the fifth day of immersion, parabolic growth of iron oxides and Fe-Cr spinel takes place.

The oxide scale, formed in the latter process, is composed of two regions, i.e., the outer iron oxide layer and the inner Fe-Cr spinel layer with different iron-chromium ratios. As shown in Figure 7i, the thickness of the outer iron oxide layer on 304SS (~3.2 µm) is almost similar to that of P91 (Figure 6i) after 15 days of immersion. For the inner part,

the concentration of iron decreases, and that of chromium increases gradually with the depth, whereas the concentration of oxygen remains consistent in this section. Further, the concentration of chromium and oxygen simultaneously shows a sharp decrease before going deep into the interface between the parent alloy and the inner oxide layer. At the same time, iron concentration increases rapidly and exceeds the alloy concentration slightly. Although the Fe-Cr spinel layer on 304SS is thinner, the higher concentration of chromium makes it more protective for the underlying substrate because of the stronger affinity of chromium to oxidants and effective hindering of the penetration of oxidants. Compared with P91, adequate storage of chromium in 304SS parent alloy assures its continuous supply to the Fe-Cr spinel layer in which a fast oxidation reaction takes place. Thus, a concentration peak of chromium (even higher than that of the parent alloy) appears at the declining point of oxygen concentration. For prolonged immersion time, the protective Fe-Cr spinel layer will provide better corrosion resistance for 304SS as compared to that of P91 as evident in Figure 3.

#### 3.4.3. IN625 Alloy

Compared with low-alloy steel and stainless steel, Ni-based alloy generally exhibits superior oxidation and corrosion resistance at high temperatures. In molten nitrate salts, many kinds of Ni-based alloys have been evaluated to pinpoint the most appropriate candidate material for CSP plants. Similar to previous studies, IN625, a representative Ni-based alloy, exhibited the best corrosion resistance among the alloys tested in this study under assimilating TES system conditions.

Figure 8 shows that the oxide films, formed on IN625 after different immersion times, are thinner and composed of smaller particles. Tiny surface oxide particles, about a few tens of nanometers in size, evolve just after 1 day of immersion. Further, the formed film is continuous in thickness on the nanometer scale. As immersion time increases, the tiny particles grow up into bigger sizes (~200 nm after 15 days of immersion) with an irregular shape. Inside the bigger particles, tiny particles generate again which seem to be growing outwards. Consequently, a compact oxide layer is formed offering hindrance to the penetration of oxidants. Apart from the slow growth of the oxide scale, no abnormal corrosion behavior is observed on most of the surface during the whole immersion test. However, the pitting corrosion phenomenon is noticed for all immersion periods as evident by Region 5 in Figure 8e. The EDS analysis of Regions 4 and 5 is summarized in Table 6 indicating that the oxides at the pitting position are rich in niobium but poor in chromium and nickel. This implies that Nb-rich regions are prone to preferential corrosion due to their lower electrode potential as compared to that of the Nb-lean matrix [41]. Therefore, galvanic corrosion could promote the oxidation of Nb-rich regions and the agglomeration of niobium oxide as evident from the corresponding XRD patterns in Figure 5. Simultaneously, the niobium content in Nb-lean regions (Region 1–3 in Figure 8) increases with the immersion time, indicating niobium oxide is probably insoluble in Solar Salt. On the contrary, chromium and molybdenum are reduced owing to their dissolution in nitrate salts which is in line with the published literature [35,48].

The thickness of the oxide scale on IN625 (~0.7 μm), immersed for 15 days, is much smaller than those of P91 (~9.2 μm) and 304SS (~6.0 μm). Moreover, it has a more compact structure and better adhesion to the parent alloy. Combining with the EDS line scanning results (Figure 8f), the oxide scale on IN625 can be divided into two parts, i.e., (I) an outer layer (which is mainly composed of nickel oxide getting rich in chromium while moving inward), and (II) an inner layer (which is composed of Ni-Cr spinel getting rich in nickel with the reduction in oxygen). Evidently, the outer nickel oxide layer (I) exhibits a lower oxidation rate and better protection effect for the inner layer (II) and the matrix when compared with the outer iron oxide layer formed on 304SS. Although the dissolution of chromium is inevitable, a sufficient amount of chromium in IN625 could provide an effective capability for the oxide scale to hinder the penetration of oxidants. Similar to the effect of Fe-Cr spinel layer formed on 304SS, the inner Ni-Cr spinel layer of IN625 results

in a sharp decrease in oxygen concentration. It is worth noting that the uphill diffusion phenomenon of chromium (as observed in the case of 304SS in Figure 7i) is not noticed. This illustrates the occurrence of a low-intensity oxidation reaction in the Ni-Cr spinel layer, which is facilitated by the downhill diffusion of chromium from the high-concentration matrix. Hence, the combination of nickel oxide and Ni-Cr spinel layers seems to be more resistant than that of iron oxide and Fe-Cr spinel layers under assimilating TES system condition of this study.

### *3.5. Salts Analysis*

Figure 9 presents a comparison of the color change and the corresponding chromium concentration in the salts after 15 days of immersion test for the three alloys. All three salts undergo a visual change from a clear (colorless) liquid to a yellow hue with different degrees, i.e., pale yellow is for P91, deep yellow is for 304SS, and chrome yellow hue (in the middle) is for IN625. As observed in Ref. [36], the yellow coloration of nitrate salts is an indication that it contains chromium. The chemical analysis results of the three exposed salts verify that the yellow color depth is correlated with chromium concentration. Compared with P91, both 304SS and IN625 suffered significant chromium dissolution (as discussed above) due to their inherent higher chromium content. Especially, during the initial stage, the matrix may directly react with salts without forming an oxide scale barrier. Thus, it is reasonable that 304SS and IN625 exhibit obvious mass loss. Unless the continuous oxide scale is formed, the dissolution of chromium is mitigated. According to the previous analysis, the differences in scale structure and growth mechanism between iron-based and nickel-based oxides may have a great influence on the corrosion process. The higher amount of chromium dissolved in salt for 304SS highlights its worse corrosion resistance than that of IN625.

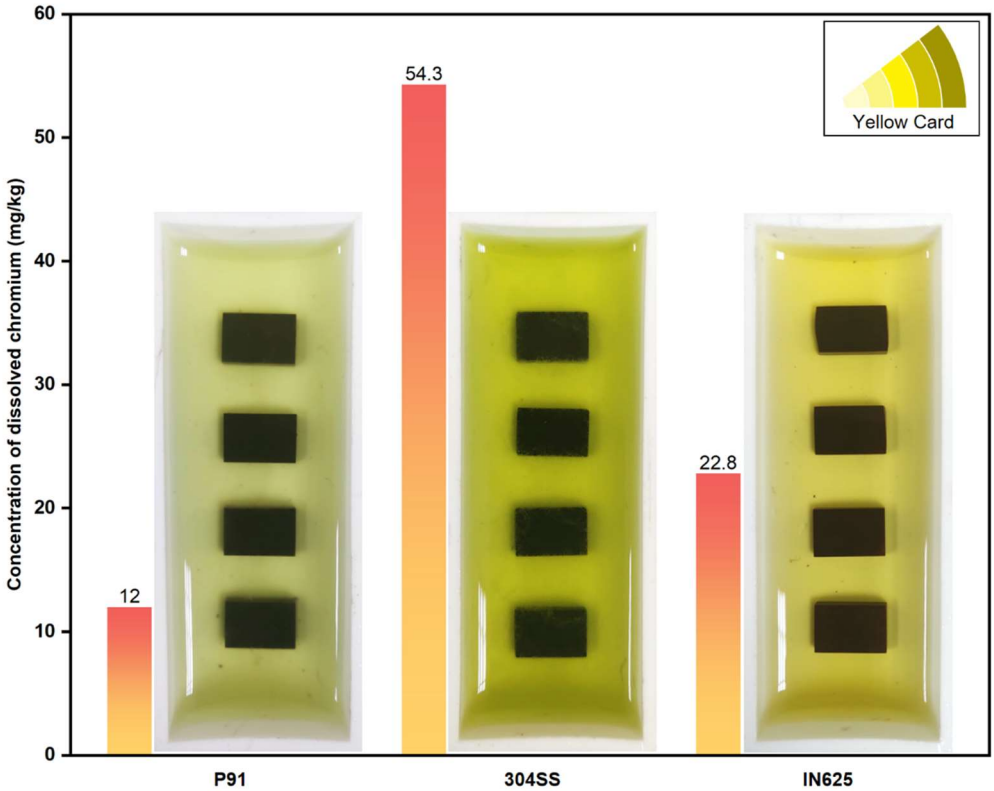


**Figure 9.** Salt samples and corresponding chromium concentration after 15 days of corrosion test for P91, 304SS, and IN625 alloys.

## 4. Corrosion Mechanisms

The corrosion of alloys in contact with Solar Salt is mainly induced by nitrate anions and impurities which can be oxygen, chlorides, and moisture. Among them, the oxygen originates from dissolved air and the thermal decomposition of nitrate anions through reaction (3) [49]. At higher temperatures, reaction (4) also contributes a negligible amount of oxygen. The secondary decomposition reactions (4) and (5) for intermediate nitrite anions describe the formation of oxide ions which may trigger the basic dissolution of metal oxides according to the Lux-Flood acid/base model [50].

$$NO_3^- \leftrightarrow NO_2^- + 1/2\ O_2 \quad (3)$$

$$2\ NO_2^- \leftrightarrow O^{2-} + 2\ NO + 1/2\ O_2 \quad (4)$$

$$2\ NO_2^- \leftrightarrow O^{2-} + NO + NO_2 \quad (5)$$

In this study, different metal elements and the corresponding contents in the three alloys resulted in different corrosion mechanisms in simulated molten Solar Salt. Based on the corrosion performance of three alloys, characterized by various analytical methods, the underlying corrosion mechanisms are discussed below. This information could not only be helpful in understanding the corrosion process of the studied three alloys under the assimilating Solar Salt condition but it might also be extended to other similar candidate alloys/coating materials to predict their corrosion behavior under TES system conditions.

### *4.1. Corrosion Mechanism of P91 Alloy*

Figure 10 illustrates the oxidation reaction standard free energy curves for the main metal elements present in the studied alloys [42]. Among these curves, iron oxides and chromium oxide are considered for P91. Figure 10 demonstrates that chromium is more prone to be oxidized thermodynamically as compared to iron. Literature suggests that $Fe_3O_4$ is the preferential iron oxide, while $Fe_2O_3$ is generally formed as a top layer on $Fe_3O_4$ under a slightly higher oxygen partial pressure [47].

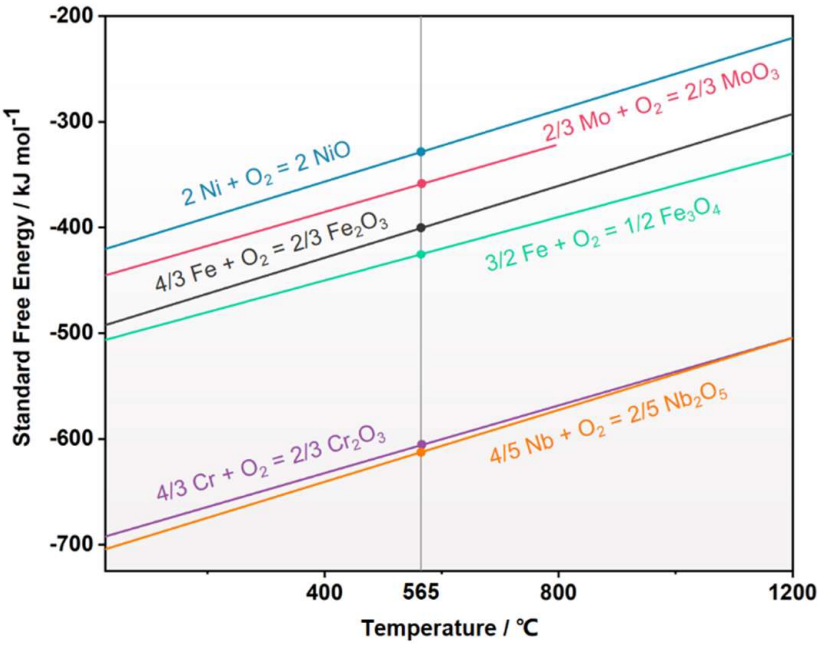


**Figure 10.** The standard formation free energy of main metal oxides formed in this study as a function of temperature.

The corrosion process for P91 in molten Solar Salt at 565 °C is schematically shown in Figure 11. During 15 days of immersion, the corrosion process can be divided into three stages, i.e., (1) initial stage, (2) oxide growth stage, and (3) internal oxidation stage. In the initial stage, both iron and chromium are oxidized as soon as the sample is exposed to molten salt through reactions (6) to (8). Due to the solid phase reaction between iron oxide and chromium oxide, such as reaction (9), Fe-Cr spinel particles appear at Cr-rich points. The FeO generally appears above 570 °C [51], therefore the generated Fe-Cr spinel is likely to be in a non-stoichiometric form ($Fe_xCr_{3-x}O_4$) at 565 °C. At the same time, chromium oxide has a risk of basic dissolution through reaction (10).

$$3/2\ Fe + O_2 \rightarrow 1/2\ Fe_3O_4 \quad (6)$$

$$4/3\ Fe + O_2 \rightarrow 2/3\ Fe_2O_3 \quad (7)$$

$$4/3\ Cr + O_2 \rightarrow 2/3\ Cr_2O_3 \quad (8)$$

$$FeO + Cr_2O_3 \rightarrow FeCr_2O_4 \quad (9)$$

$$Cr_2O_3 + 2\ O^{2-} + 3/2\ O_2 \rightarrow 2\ CrO_4^{2-} \quad (10)$$

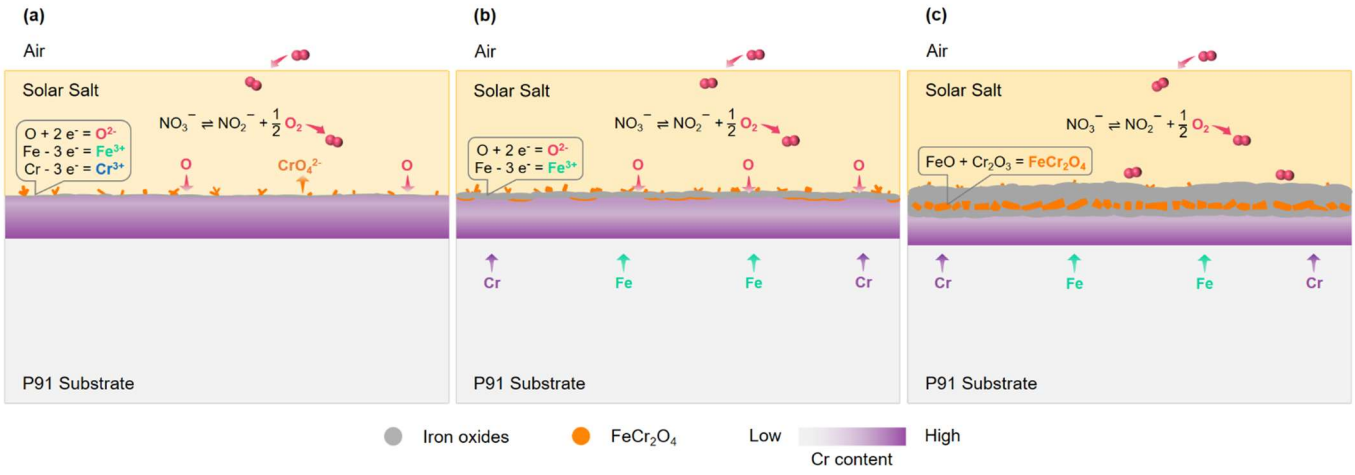


**Figure 11.** Schematic of the corrosion process of P91 alloy exposed to Solar Salt at 565 °C for 15 days. (**a**) Initial stage, (**b**) Oxide growth stage, (**c**) Internal oxidation stage.

During the oxide growth stage, the iron oxides grow rapidly and become the outer oxide scale because of the lower content and diffusion speed of chromium as compared to those of iron in the substrate. Along with the outward diffusion of iron ions, oxide ions gradually diffuse inward to the substrate/oxides interface and cause internal oxidation. Chromium oxides nucleate preferentially at Cr-rich regions and further grow in size through the aggregation of chromium ions migrating from the inner matrix.

During the internal oxidation stage, the lack of a quick and adequate supply of Cr in this low-chromium alloy, iron oxides evolve around chromium oxides and subsequently mix with the latter thereby producing discontinuous Fe-Cr spinel islands. The Fe-Cr spinel is considered to be protective in molten nitrate salts and high temperature oxidation environments for blocking the migration of iron and oxide ions. However, the blocking effect of Fe-Cr spinel islands is not effective in the present condition. Oxide ions may penetrate through the mixed oxide layer and react with adjacent Cr-depleted regions thus resulting in the formation of the inner iron oxide layer. Therefore, the oxide scales on P91 will have a sandwich structure that is composed of an outward-growing iron oxide layer,

an intermediate mixed Fe-Cr spinel layer, and an inner iron oxide layer. If there is no spallation of oxide scales, it can be assumed that an alternating multilayered structure of iron oxide and mixed Fe-Cr spinel will be formed during prolonged immersion.

### *4.2. Corrosion Mechanism of 304SS Alloy*

304SS, another kind of Fe-based alloy with a relatively high content of chromium and other alloying elements (such as nickel, manganese, etc.), shows a different corrosion mechanism as compared to that of P91. Figure 12 demonstrates the corrosion process for 304SS during 15 days of immersion which can be divided into an earlier corrosion period (a–c) and a later corrosion period (d–f).

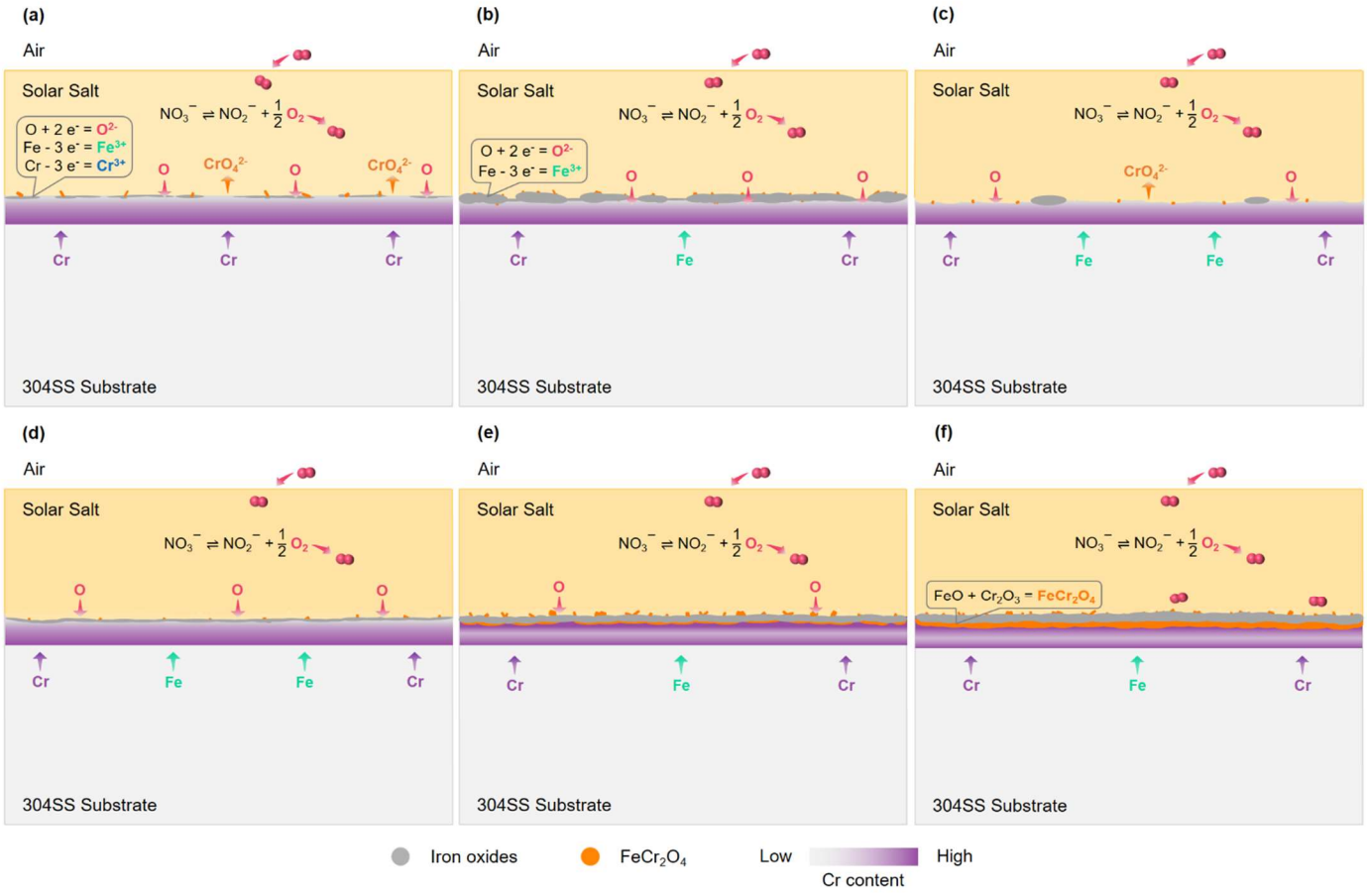


**Figure 12.** Schematic of the corrosion process of 304SS alloy exposed to Solar Salt at 565 °C for 15 days. (**a**–**c**) Earlier corrosion period, (**d**–**f**) Later corrosion period.

The earlier corrosion period (Figure 12a–c) is a short and rapid reaction process, which could be further divided into three stages, i.e., (1) chromium dissolution, (2) iron oxide generation, and (3) peeling off of iron oxide layer. At the chromium dissolution stage, the high content of chromium in 304SS makes the dissolution effect more evident as the sample surface makes contact with molten nitrate salts. Besides the indirect dissolution by reactions (8) and (10), a great amount of chromium could directly react with nitrate ions, generating soluble chromate ions through reactions (11) and (12) [35,52]. The massive dissolution of chromium in a short time increases the vacancy concentration in the surface layer and provides oxidants more access to penetrate into the alloy. Meanwhile, excessive depletion of surface chromium may trigger outward diffusion of chromium from the internal matrix. During the oxide generation stage, the non-dissolved iron is instantly oxidized in situ with the help of penetrating oxygen. Thanks to the high concentration of vacancy at the surface, iron ions may easily migrate outward during this stage. Hence, the iron oxide layer is formed at a remarkable rate. During the stage of peeling off of the iron oxide layer, the

rapid growth of iron oxides may induce stress between the oxide layer and the underlying matrix. As the new oxides nucleate and grow on the interface, the iron oxide layer may gradually peel off thereby exposing a fresh surface. At this moment, the surface condition of the 304SS is similar to that of P91 based on the iron-chromium concentration ratio and morphology of oxides.

$$2\,Cr + 7\,NO_3^- \rightarrow 2\,CrO_4^{2-} + 3\,NO_2^- + 3\,NO_2 + NO \quad (11)$$

$$Cr + 2\,NO_3^- \rightarrow CrO_4^{2-} + 2NO \quad (12)$$

In the later stages of corrosion (Figure 12d–f), it is expected that 304SS may be corroded in the same way as P91 did (Figure 11). Here, the iron oxide scale is formed again but with a slower growth rate as compared to that in the earlier corrosion period. This is due to the fact that no excessive chromium dissolution takes place at its lower concentration and the diffusion of iron and oxide ions gets slowed down. In the next stage, chromium oxides and Fe-Cr spinel are formed beneath the outer iron oxide layer. Owing to the adequate supply of chromium from the inner matrix, a continuous Fe-Cr spinel layer appears as an inner oxide layer. With the thickening of the Fe-Cr spinel layer, the migration-blocking effect of iron and oxide ions would become more evident. Further, no inner iron oxide layer would be found and the growth rate of the outer iron oxide layer would decrease gradually. For longer immersion time, the oxide scale would provide good corrosion resistance to 304SS.

### *4.3. Corrosion Mechanism of IN625 Alloy*

Figure 13 schematically presents the corrosion mechanism for IN625 containing a high content of chromium and molybdenum. Compared with 304SS, the corrosion process of IN625 is simpler and proceeds much more slowly. Since IN625 is richer in chromium, the direct dissolution of chromium by reactions (11) and (12) may take place again at the initial stage in the same manner as 304SS. Contrary to the oxidation process of iron, nickel is oxidized slowly through reaction (13) and the resulting nickel oxide layer is relatively thinner and denser. After forming a continuous nickel oxide layer, the dissolution of chromium and the penetration of oxygen are hindered.

$$2\,Ni + O_2 \rightarrow 2\,NiO \quad (13)$$

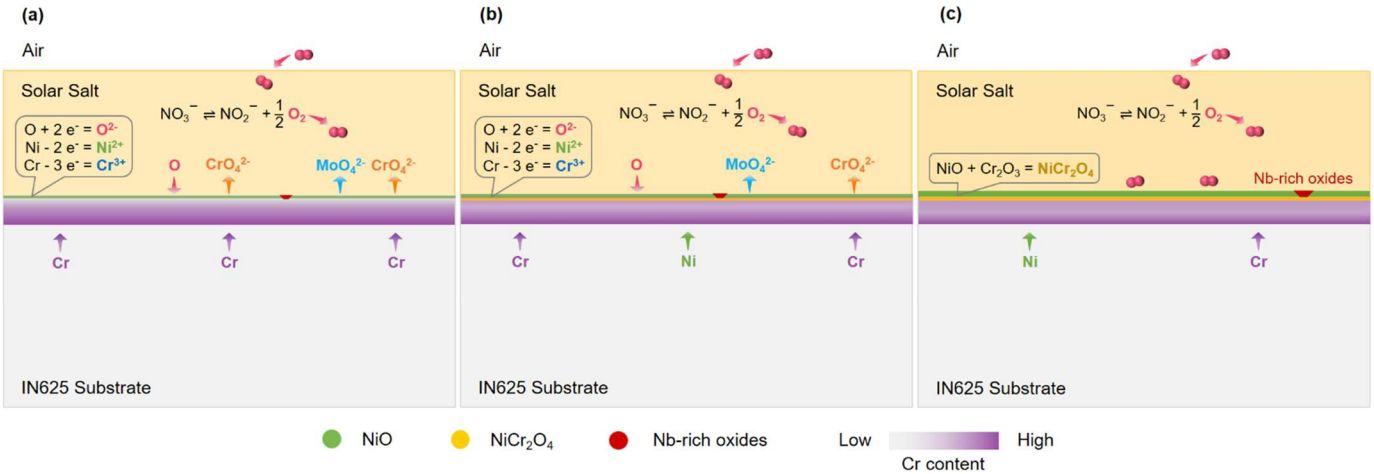


**Figure 13.** (**a**–**c**) Schematic of the corrosion process of IN625 alloy exposed to Solar Salt at 565 °C for 15 days.

Apart from the oxidation of nickel and chromium, molybdenum and niobium would also be oxidized through reactions (14) and (15). Figure 10 suggests that niobium has the highest oxidation potential among the constituent elements of IN625, therefore Nb-rich re-

gions are prone to be oxidized preferentially resulting in the pitting corrosion phenomenon. Further, molybdenum oxide could be dissolved into basic molten salts through reaction (17), which means that it is disadvantageous for the generation of a continuous and compact oxide layer. As immersion time increases, the nickel oxide layer becomes thicker through the outward diffusion of nickel ions and the inward penetration of oxide ions. Underneath the nickel oxide layer, the solid phase reaction (16) between nickel oxide and chromium oxide would take place, thus resulting in the formation of Ni-Cr spinel which has superior corrosion resistance. After forming a continuous spinel layer, the rate of internal oxidation and growth of nickel oxide would become slower while the dissolution of chromium and molybdenum would be further alleviated. Hence, the compact and corrosion-resistant products make IN625 a suitable choice for TES components which could maintain contact with molten Solar Salt (at 565 °C) for a prolonged time.

$$2/3\ \mathrm{Mo} + \mathrm{O_2} \rightarrow 2/3\ \mathrm{MoO_3} \tag{14}$$

$$4/5\ \mathrm{Nb} + \mathrm{O_2} \rightarrow 2/5\ \mathrm{Nb_2O_5} \tag{15}$$

$$\mathrm{NiO} + \mathrm{Cr_2O_3} \rightarrow \mathrm{NiCr_2O_4} \tag{16}$$

$$\mathrm{MoO_3} + \mathrm{O^{2-}} \rightarrow \mathrm{MoO_4^{2-}} \tag{17}$$

## 5. Summary and Conclusions

In this work, the corrosion behavior of three kinds of engineering alloys (P91, 304SS and IN625) was evaluated in Solar Salt at 565 °C for up to 15 days. The evolution of corrosion products was studied in detail using gravimetric, macroscopic, SEM and XRD techniques. Chemical analysis of exposed salts for three alloys was conducted by ICP-MS. Based on the corrosion performance of studied alloys and analytical results, the possible corrosion mechanisms were discussed in detail. The main conclusions of this study are summarized as follows:

(1) During 15 days of immersion test, IN625 shows the best corrosion resistance with the lowest corrosion rate (2.27 μm/a), followed by P91 (31.84 μm/a) and 304SS (72.16 μm/a). For longer-term immersion, 304SS is expected to be more corrosion-resistant than P91, and the latter may face a risk of breakaway corrosion.

(2) The oxide scale on P91 is composed of an outer iron oxide layer, an inner iron oxide layer, and an intermediate mixed Fe-Cr spinel layer in which Fe-Cr spinel is discontinuous due to less outward diffusion of chromium from the parent alloy. Other low-chromium alloys are expected to exhibit a similar corrosion behavior and are not recommended for direct use as TES components.

(3) 304SS suffered significant dissolution of chromium and rapid growth of iron oxides in the initial period of the immersion test. After early fluctuation, the newly formed oxide scale became thinner and more compact with a duplex structure ($Fe_2O_3$ as an outer layer and $FeCr_2O_4$ as an inner layer). The corrosion resistance of 304SS is remarkably improved due to the formation of a continuous Fe-Cr spinel layer.

(4) IN625 experienced evident mass loss due to the dissolution of chromium at the beginning. After forming a continuous NiO layer, the dissolution phenomenon was mitigated. Further, Ni-Cr spinel inner layer effectively impeded the internal oxidation. However, pitting corrosion took place in Nb-rich regions which need special attention to avoid local failure.

(5) For P91, oxidation and dissolution of chromium are supposed to occur simultaneously. For 304SS and IN625, rapid dissolution of chromium could cause evident mass loss and change surface structure/composition. Since iron alloys are more economical than nickel alloys, with some surface treatments, e.g., reducing the superficial content

of chromium for 304SS or depositing compact and resistant coating (such as Ni-based materials) on P91, the iron alloys may be the superior choice for TES components.

**Author Contributions:** Conceptualization, X.C.; Data curation, N.L.; Formal analysis, N.L.; Investigation, N.L., B.H. and R.H.; Methodology, N.L., N.u.H.T., J.W., X.C. and T.X.; Resources, X.C. and T.X.; Supervision, J.W., X.C. and T.X.; Visualization, N.L. and N.u.H.T.; Writing—original draft, N.L.; Writing—review & editing, N.u.H.T., B.H. and R.H. All authors have read and agreed to the published version of the manuscript.

**Funding:** This research received no external funding.

**Data Availability Statement:** The raw/processed data required to reproduce these findings are directly presented in the paper and therefore they are immediately accessible.

**Acknowledgments:** This research did not receive any specific grant from funding agencies in the public, commercial, or not-for-profit sectors. The authors would like to express their thanks to Jing Luo for her valuable advice and guidance.

**Conflicts of Interest:** The authors declare no conflict of interest.

## References

1. Fernández, A.G.; Gomez-Vidal, J.; Oró, E.; Kruizenga, A.; Solé, A.; Cabeza, L.F. Mainstreaming commercial CSP systems: A technology review. *Renew. Energy* **2019**, *140*, 152–176. [CrossRef]
2. Islam, M.T.; Huda, N.; Abdullah, A.B.; Saidur, R. A comprehensive review of state-of-the-art concentrating solar power (CSP) technologies: Current status and research trends. *Renew. Sustain. Energy Rev.* **2018**, *91*, 987–1018. [CrossRef]
3. Gil, A.; Medrano, M.; Martorell, I.; Lázaro, A.; Dolado, P.; Zalba, B.; Cabeza, L.F. State of the art on high temperature thermal energy storage for power generation. Part 1—Concepts, materials and modellization. *Renew. Sustain. Energy Rev.* **2010**, *14*, 31–55. [CrossRef]
4. Palacios, A.; Barreneche, C.; Navarro, M.; Ding, Y. Thermal energy storage technologies for concentrated solar power—A review from a materials perspective. *Renew. Energy* **2020**, *156*, 1244–1265. [CrossRef]
5. Tian, Y.; Zhao, C. A review of solar collectors and thermal energy storage in solar thermal applications. *Appl. Energy* **2013**, *104*, 538–553. [CrossRef]
6. Giaconia, A.; Tizzoni, A.C.; Sau, S.; Corsaro, N.; Mansi, E.; Spadoni, A.; Delise, T. Assessment and Perspectives of Heat Transfer Fluids for CSP Applications. *Energies* **2021**, *14*, 7486. [CrossRef]
7. Bhatnagar, P.; Siddiqui, S.; Sreedhar, I.; Parameshwaran, R. Molten salts: Potential candidates for thermal energy storage applications. *Int. J. Energy Res.* **2022**, *46*, 17755–17785. [CrossRef]
8. Vignarooban, K.; Xu, X.; Arvay, A.; Hsu, K.; Kannan, A. Heat transfer fluids for concentrating solar power systems—A review. *Appl. Energy* **2015**, *146*, 383–396. [CrossRef]
9. Mehos, M.; Turchi, C.; Vidal, J.; Wagner, M.; Ma, Z.; Ho, C.; Kolb, W.; Andraka, C.; Kruizenga, A. *Concentrating Solar Power Gen3 Demonstration Roadmap*; No. NREL/TP-5500-67464; National Renewable Energy Lab. (NREL): Golden, CO, USA, 2017.
10. Pacheco, J.E.; Bradshaw, R.W.; Dawson, D.B.; De la Rosa, W.; Gilbert, R.; Goods, S.H.; Hale, M.J.; Jacobs, P.; Jones, S.A.; Kolb, G.J.; et al. *Final Test and Evaluation Results from the Solar Two Project*; No. SAND2002-0120; Sandia National Lab. (SNL-NM): Albuquerque, NM, USA; Sandia National Lab. (SNL-CA): Livermore, CA, USA, 2002.
11. Ma, L.; Zhang, C.; Wu, Y.; Lu, Y. Comparative review of different influence factors on molten salt corrosion characteristics for thermal energy storage. *Sol. Energy Mater. Sol. Cells* **2022**, *235*, 111485. [CrossRef]
12. Tortorelli, P.F.; Bishop, P.S.; DiStefano, J.R. *Selection of Corrosion-Resistant Materials for Use in Molten Nitrate Salts*; No. ORNL/TM-11162; Oak Ridge National Lab.: Oak Ridge, TN, USA, 1989.
13. Ruiz-Cabañas, F.J.; Prieto, C.; Madina, V.; Fernández, A.I.; Cabeza, L.F. Materials selection for thermal energy storage systems in parabolic trough collector solar facilities using high chloride content nitrate salts. *Sol. Energy Mater. Sol. Cells* **2017**, *163*, 134–147. [CrossRef]
14. Baraka, A.; Abdel-Rohman, A.I.; Hosary, A.A.E. Corrosion of mild steel in molten sodium nitrate–potassium nitrate eutectic. *Br. Corros. J.* **1976**, *11*, 44–46. [CrossRef]
15. García-Martín, G.; Lasanta, M.; Encinas-Sánchez, V.; de Miguel, M.; Pérez, F. Evaluation of corrosion resistance of A516 Steel in a molten nitrate salt mixture using a pilot plant facility for application in CSP plants. *Sol. Energy Mater. Sol. Cells* **2017**, *161*, 226–231. [CrossRef]
16. Ruiz-Cabañas, F.J.; Prieto, C.; Osuna, R.; Madina, V.; Fernández, A.I.; Cabeza, L.F. Corrosion testing device for in-situ corrosion characterization in operational molten salts storage tanks: A516 Gr70 carbon steel performance under molten salts exposure. *Sol. Energy Mater. Sol. Cells* **2016**, *157*, 383–392. [CrossRef]

17. Nieto-Maestre, J.; Muñoz-Sánchez, B.; Fernández, A.G.; Faik, A.; Grosu, Y.; García-Romero, A. Compatibility of container materials for Concentrated Solar Power with a solar salt and alumina based nanofluid: A study under dynamic conditions. *Renew. Energy* **2020**, *146*, 384–396. [CrossRef]
18. Fernández, A.; Galleguillos, H.; Fuentealba, E.; Pérez, F. Corrosion of stainless steels and low-Cr steel in molten $Ca(NO_3)_2$–$NaNO_3$–$KNO_3$ eutectic salt for direct energy storage in CSP plants. *Sol. Energy Mater. Sol. Cells* **2015**, *141*, 7–13. [CrossRef]
19. Dorcheh, A.S.; Galetz, M. Slurry aluminizing: A solution for molten nitrate salt corrosion in concentrated solar power plants. *Sol. Energy Mater. Sol. Cells* **2016**, *146*, 8–15. [CrossRef]
20. Encinas-Sánchez, V.; de Miguel, M.; Lasanta, M.; García-Martín, G.; Perez-Trujillo, F.J. Electrochemical impedance spectroscopy (EIS): An efficient technique for monitoring corrosion processes in molten salt environments in CSP applications. *Sol. Energy Mater. Sol. Cells* **2019**, *191*, 157–163. [CrossRef]
21. Mallco, A.; Pineda, F.; Mendoza, M.; Henriquez, M.; Carrasco, C.; Vergara, V.; Fuentealba, E.; Fernandez, A.G. Evaluation of flow accelerated corrosion and mechanical performance of martensitic steel T91 for a ternary mixture of molten salts for CSP plants. *Sol. Energy Mater. Sol. Cells* **2022**, *238*, 111623. [CrossRef]
22. Pineda, F.; Walczak, M.; Vilchez, F.; Guerra, C.; Escobar, R.; Sancy, M. Evolution of corrosion products on ASTM A36 and AISI 304L steels formed in exposure to molten NaNO3–KNO3 eutectic salt: Electrochemical study. *Corros. Sci.* **2022**, *196*, 110047. [CrossRef]
23. Gomes, A.; Navas, M.; Uranga, N.; Paiva, T.; Figueira, I.; Diamantino, T. High-temperature corrosion performance of austenitic stainless steels type AISI 316L and AISI 321H, in molten Solar Salt. *Sol. Energy* **2019**, *177*, 408–419. [CrossRef]
24. Ma, L.; Zhang, C.; Wu, Y.; Lu, Y.; Ma, C. Dynamic corrosion behavior of 316L stainless steel in quaternary nitrate-nitrite salts under different flow rates. *Sol. Energy Mater. Sol. Cells* **2020**, *218*, 110821. [CrossRef]
25. Gao, Q.; Lu, Y.; Yu, Q.; Wu, Y.; Zhang, C.; Zhi, R. High-temperature corrosion behavior of austenitic stainless steel in quaternary nitrate molten salt nanofluids for concentrated solar power. *Sol. Energy Mater. Sol. Cells* **2022**, *245*, 111851. [CrossRef]
26. Elbakhshwan, M.; Lee, D.H.; Anderson, M. Corrosion resistance of high nickel alloys in solar salt at 600 °C for up to 4000 h. *Sol. Energy Mater. Sol. Cells* **2022**, *245*, 111837. [CrossRef]
27. Palacios, A.; Navarro, M.E.; Jiang, Z.; Avila, A.; Qiao, G.; Mura, E.; Ding, Y. High-temperature corrosion behaviour of metal alloys in commercial molten salts. *Sol. Energy* **2020**, *201*, 437–452. [CrossRef]
28. Gomez-Guzman, N.B.; Lopez-Dominguez, D.; Arrieta-Gonzalez, C.D.; Mayen, J.; Porcayo-Palafox, E.; Chacon-Nava, J.G.; Gonzalez-Rodriguez, J.G.; Porcayo-Calderon, J.; Rodriguez-Diaz, R.A. Behavior of Ni20Cr Alloy in Molten Nitrate Salts. *Int. J. Mol. Sci.* **2022**, *23*, 7895. [CrossRef]
29. Liu, C.; Tang, X.; Cheng, L.; Leng, B.; Li, X.; Ye, X.-X.; Huang, H. The characterization of corrosion layers of GH3535 and Inconel 625 alloys in molten $KNO_3$-$NaNO_3$ salts at 500 °C. *Corros. Sci.* **2022**, *204*, 110406. [CrossRef]
30. Dorcheh, A.S.; Durham, R.N.; Galetz, M.C. Corrosion behavior of stainless and low-chromium steels and IN625 in molten nitrate salts at 600 °C. *Sol. Energy Mater. Sol. Cells* **2016**, *144*, 109–116. [CrossRef]
31. Prieto, C.; Ruiz-Cabañas, F.J.; Madina, V.; Fernández, A.I.; Cabeza, L.F. Corrosion performance of alloy 800H and alloy 625 for potential use as molten salts solar receiver materials in concentrating solar power tower plants. *J. Energy Storage* **2022**, *55*, 105824. [CrossRef]
32. Teeter, L.; Adam, B.; Wood, T.; Tucker, J. Comparison of the corrosion of materials in supercritical carbon dioxide, air, and argon environments. *Corros. Sci.* **2021**, *192*, 109752. [CrossRef]
33. Kuang, W.; Wu, X.; Han, E.-H. The oxidation behaviour of 304 stainless steel in oxygenated high temperature water. *Corros. Sci.* **2010**, *52*, 4081–4087. [CrossRef]
34. Jafari, R.; Sadeghi, E. High-temperature corrosion performance of HVAF-sprayed NiCr, NiAl, and NiCrAlY coatings with alkali sulfate/chloride exposed to ambient air. *Corros. Sci.* **2019**, *160*, 108066. [CrossRef]
35. Meißner, T.M.; Oskay, C.; Bonk, A.; Grégoire, B.; Donchev, A.; Solimani, A.; Galetz, M.C. Improving the corrosion resistance of ferritic-martensitic steels at 600 °C in molten solar salt via diffusion coatings. *Sol. Energy Mater. Sol. Cells* **2021**, *227*, 111105. [CrossRef]
36. Summers, K.L.; Chidambaram, D. Corrosion Behavior of Structural Materials for Potential Use in Nitrate Salts Based Solar Thermal Power Plants. *J. Electrochem. Soc.* **2017**, *164*, H5357–H5363. [CrossRef]
37. Walczak, M.; Pineda, F.; Fernández, G.; Mata-Torres, C.; Escobar, R.A. Materials corrosion for thermal energy storage systems in concentrated solar power plants. *Renew. Sustain. Energy Rev.* **2018**, *86*, 22–44. [CrossRef]
38. Standard, ASTM. *Standard Practice for Preparing, Cleaning, and Evaluating Corrosion Test Specimens*; American Society for Testing and Materials G1-03; ASTM International: West Conshohocken, PA, USA, 2011.
39. Zhang, X.; Zhang, C.; Wu, Y.; Lu, Y. Experimental research of high temperature dynamic corrosion characteristic of stainless steels in nitrate eutectic molten salt. *Sol. Energy* **2020**, *209*, 618–627. [CrossRef]
40. Rapp, R.A.; Goto, K.S. The hot corrosion of metals by molten salts. *ECS Proc. Vol.* **1981**, *10*, 159–177. [CrossRef]
41. Vanysek, P. Electrochemical series. In *CRC Handbook of Chemistry and Physics*, 87th ed.; CRC Press: Boca Raton, FL, USA, 1998.
42. University of Cambridge Website. The Interactive Ellingham Diagram. Available online: https://www.doitpoms.ac.uk (accessed on 24 October 2022).
43. Liu, Q.; Barker, R.; Wang, C.; Qian, J.; Neville, A.; Pessu, F. The corrosion behaviour of stainless steels and Ni-based alloys in nitrate salts under thermal cycling conditions in concentrated solar power plants. *Sol. Energy* **2022**, *232*, 169–185. [CrossRef]

44. Parizia, S.; Marchese, G.; Rashidi, M.; Lorusso, M.; Hryha, E.; Manfredi, D.; Biamino, S. Effect of heat treatment on microstructure and oxidation properties of Inconel 625 processed by LPBF. *J. Alloys Compd.* **2020**, *846*, 156418. [CrossRef]
45. Hu, H.; Zhou, Z.; Li, M.; Zhang, L.; Wang, M.; Li, S.; Ge, C. Study of the corrosion behavior of a 18Cr-oxide dispersion strengthened steel in supercritical water. *Corros. Sci.* **2012**, *65*, 209–213. [CrossRef]
46. Gurr, M.; Bau, S.; Burmeister, F.; Wirth, M.; Piedra-Gonzalez, E.; Krebser, K.; Preußner, J.; Pfeiffer, W. Investigation of the corrosion behavior of NiVAl multilayer coatings in hot salt melts. *Surf. Coat. Technol.* **2015**, *279*, 101–111. [CrossRef]
47. Jonsson, T.; Pujilaksono, B.; Heidari, H.; Liu, F.; Svensson, J.-E.; Halvarsson, M.; Johansson, L.-G. Oxidation of Fe–10Cr in $O_2$ and in $O_2$+$H_2O$ environment at 600 °C: A microstructural investigation. *Corros. Sci.* **2013**, *75*, 326–336. [CrossRef]
48. Xie, W.; Ding, J.; Wei, X.; Wang, W.; Xia, G.; Xing, J. Corrosion Resistance of Stainless Steel and Pure Metal in Ternary Molten Nitrate for Thermal Energy Storage. *Energy Procedia* **2019**, *158*, 4897–4902. [CrossRef]
49. Sötz, V.A.; Bonk, A.; Forstner, J.; Bauer, T. Microkinetics of the reaction $NO_3$- ⇌ $NO_2$- + 0.5 $O_2$ in molten sodium nitrate and potassium nitrate salt. *Thermochim. Acta* **2019**, *678*, 178301. [CrossRef]
50. Flood, H.; Förland, T. The acidic and basic properties of oxides. *Acta Chem. Scand.* **1947**, *1*, 592–606. [CrossRef] [PubMed]
51. Birks, N.; Meier, G.H.; Pettit, F.S. *Introduction to the High-Temperature Oxidation of Metals*; Cambridge University Press: Cambridge, UK, 2006; pp. 75–100.
52. Olivares, R.I. The thermal stability of molten nitrite/nitrates salt for solar thermal energy storage in different atmospheres. *Sol. Energy* **2012**, *86*, 2576–2583. [CrossRef]